Supporting Information

Machine Learning-Accelerated Discovery of Multi-Cation Entropy-Stabilized NASICON Solid Electrolytes with 10,000 Hours of Stable Na Plating/Stripping for All-Solid-State Sodium Batteries

Authors: Daxian Zuo,‡[ab] Jiaming Tian,‡[a] Yu Sun,‡[a] Xin Yu,[a] Bo Peng,[a] Tao Yu,[ab] Chengrong Xu,[ab] Xiangqun Xu,[ab] Yigang Wang,[a] Yiwen Liu,[a] Tianze Shi,[a] Yinhui Feng,[a] Jie Yang,[a] Haoshen Zhou[a], and Shaohua Guo*[ab]

Address:

[a] College of Engineering and Applied Sciences, Jiangsu Key Laboratory of Artificial Functional Materials, National Laboratory of Solid-State Microstructures, Collaborative Innovation Center of Advanced Microstructures, Nanjing University, Nanjing, 210093, China

[b] Lab of Power and Energy Storage Batteries, Shenzhen Research Institute of Nanjing University, Shenzhen, 518000, China

‡ These authors contributed equally to this work.

* Corresponding Email： shguo@nju.edu.cn

Methods

Machine learning

This study utilized the Python programming language and the scikit-learn machine learning library to conduct classification training on 5 ML models. The performance of these models was rigorously evaluated using a variety of metrics, including accuracy, recall, and precision. Additionally, the models' discriminatory power was assessed through the analysis of the receiver operating characteristic (ROC) curve and the corresponding confusion matrix, which allowed for a comprehensive evaluation of their classification performance. To frame the problem for classification, the synthesis outcomes of medium- and high-entropy solid-state electrolytes were reformulated into a binary classification task. This involved compiling the synthesis data for 58 solid-state electrolytes and categorizing each result as either a successful synthesis (denoted by '1') or a failed synthesis (denoted by '0'). This binary dataset was then utilized to train the machine learning models, enabling them to learn the underlying patterns and relationships that distinguish between successful and unsuccessful synthesis outcomes.

Materials Synthesis

All the compounds studied in this work were synthesized by solid-state reaction. Metal oxides (CaO, ZnO, MgO, Ga_2O_3, Y_2O_3, Bi_2O_3, Al_2O_3, Sc_2O_3, In_2O_3, Nd_2O_3, Er_2O_3, Tm_2O_3, Lu_2O_3, ZrO_2, SnO_2, HfO_2, GeO_2, CeO_2, IrO_2, TiO_2, Ta_2O_5, MoO_3, WO_3) were used to provide metal cations. The oxides (99.9%, Sigma Aldrich) were used as purchased, which were preheated at 900 °C to decompose any carbonate or hydroxide impurities. Na_2CO_3 (99.9%, Sigma Aldrich) were used to introduce Na ions. $NH_4H_2PO_4$ (99.9%, Sigma Aldrich) and SiO_2 (99.9%, Sigma Aldrich) was used to introduce PO_4 and SiO_4. 10 wt.% excess of Na_2CO_3 and $NH_4H_2PO_4$ was used to compensate for Na and P loss during high-temperature annealing. In a typical synthesis, the required precursors were mixed with anhydrous ethanol in a planetary ball mill (Pulverisette 6, Fritsch) using yttria-stabilized zirconia (YSZ) milling jars and balls. The ball-to-powder weight ratio was maintained at 20:1. The mixture was milled at 500 rpm for 12 h. The slurry was dried at 80 ℃ and then preheated at 900 ℃ for 12 h. Then, the obtained solids were ground using a mortar and pestle, pelletized, and heated at 1100-1200 ℃ for 12 h, finished by a controlled cooling rate of 2℃ min^{-1} in the air and grinding to obtain powders for further

characterizations. For the different NASICON oxide SSEs, the as-prepared pellets were polished with 1000, 2000, and 5000 mesh sandpapers and stored in a glovebox for electrochemical tests.

Materials characterizations

X-ray diffraction (XRD) data of the different NASICON oxide powders were measured by a Bruker D8 Advance diffractometer (Germany) under room temperature, and the testing was completed under the protection of an argon atmosphere. The Rietveld refinements were performed to obtain the detailed crystal structures by the GSAS program on the EXPGUI interface. Scanning electron microscope (SEM) images were performed with a Sigma 300 field emission SEM instrument. For the transmission electron microscopy (TEM) investigation, the samples were thoroughly ground into powders and diluted in ethanol by ultrasonic treatment for 5 min. The suspension liquid was dripped onto holey carbon-coated Cu grids. The high-angle annular dark-field scanning transmission electron microscopy (HAADF-STEM) and energy dispersive spectroscopy (EDS) experiments were performed using an FEI Talos F200X G2 microscope equipped with Bruker windowless EDX detector at an accelerating voltage of 200 KV.

Conductivity measurements

To measure ionic conductivities, the as-synthesized powders were pressed into pellets (10 mm diameter) and sintered under air at 1100 ℃, followed by fast air cooling. The sintered pellets were sputtered with a thin layer of Au on each side to form good contact between the Au metal and the NASICON oxide pellets. AC impedance measurements were performed at room temperature using a Biologic VSP-300 potentiostat. A frequency range of 1 MHz to 1 Hz and an excitation voltage of 10 mV were applied during the measurements. Ionic conductivity was calculated based on the following Equation: $\sigma_t = L/(R_tS)$, where σ_t, L, S, and R_t represent the ionic conductivity, thickness of electrolyte pellets, electrolyte pellet surface area, and resistance value. Activation energies were calculated from the slope of the resulting Arrhenius plot. Electronic conductivity was examined by DC polarization experiment with a DC voltage of 0.5 V.

Na||Na symmetric cell fabrication and measurement

To ensure optimal interfacial contact between the sodium metal electrodes and the NASICON solid electrolyte, a Sn interlayer was deposited on both surfaces of the electrolyte pellet via magnetron sputtering. Subsequently, Na foils with a diameter of 9 mm were symmetrically attached to the Sn-coated surfaces. All cell assembly procedures were performed in an Ar-filled glovebox maintaining H_2O and O_2 levels below 0.1 ppm. The electrochemical performance of the symmetric cells was evaluated using CR2032 coin-type configurations. Galvanostatic sodium stripping/plating tests were conducted at room temperature with a constant current density of 0.1 mA cm^{-2}. The critical current density of the solid electrolyte was determined using Na|SSEs|Na symmetric cells through a stepwise current cycling protocol. Measurements were performed on an automated battery testing system (NEWARE Battery Test System [CT-4008T-5V10mA-164, Shenzhen, China]) with an initial current density of 0.1 mA cm^{-2}, incrementally increased by 0.1 mA cm^{-2} per step until cell failure occurred.

Na||NVPF full cell fabrication and measurement

The CR2032-type ASSSBs were assembled using a NVPF-plastic crystal electrolyte (PCE) composite cathode, a sodium metal foil anode, and a NASICON-type solid electrolyte. A Sn interlayer was deposited onto the surface of the electrolyte pellet using magnetron sputtering. All cell assembly procedures were carried out in an argon-filled glovebox with H_2O and O_2 levels below 0.1 ppm. The PCE was prepared as a deformable ionic conductor by dissolving 0.1 mmol $NaClO_4$ in 2 mmol succinonitrile at 65 °C, forming a homogeneous viscous yellow electrolyte upon cooling.[1,2] This design allows it to serve as a dynamic interfacial buffer in the cathode composite. The NVPF-PCE composite cathode was fabricated by mixing NVPF nanoplates, carbon black, PVDF binder, and PCE (60:5:10:25 wt%) in N-methyl-2-pyrrolidone (NMP), followed by slurry casting onto aluminum foil, vacuum drying, and punching into 9-mm discs (1.5 mg cm^{-2} active mass loading). Galvanostatic charging/discharging (NEWARE Battery Test System [CT-4008T-5V10mA-164, Shenzhen, China]) of the cells was conducted in the voltage range of 2.0-4.3 V (vs Na/Na^+) at room temperature.

DFT and BVSE calculations

The all DFT calculations were carried out using the Vienna Ab initio Simulation Package (VASP). We used the generalized gradient approximation of Perdew-Burke-Ernzerhof (GGA-

PBE) exchange-correlational functional and the projector-augmented wave method at the generalized gradient approximation level. A cutoff energy of 550 eV was set for all calculations. The total energy convergence and the forces on each atom were set to be 10^{-5} eV and 0.03 eV $Å^{-1}$. BVSE calculations were performed by means of the softBV-GUI program. To calculate the energy of ion sites in the structure, a three-dimensional grid with a resolution of 0.1 Å and a screening factor of 0.75 was used. The crystal structure and potential isosurfaces of the calculations were visualized using VESTA.

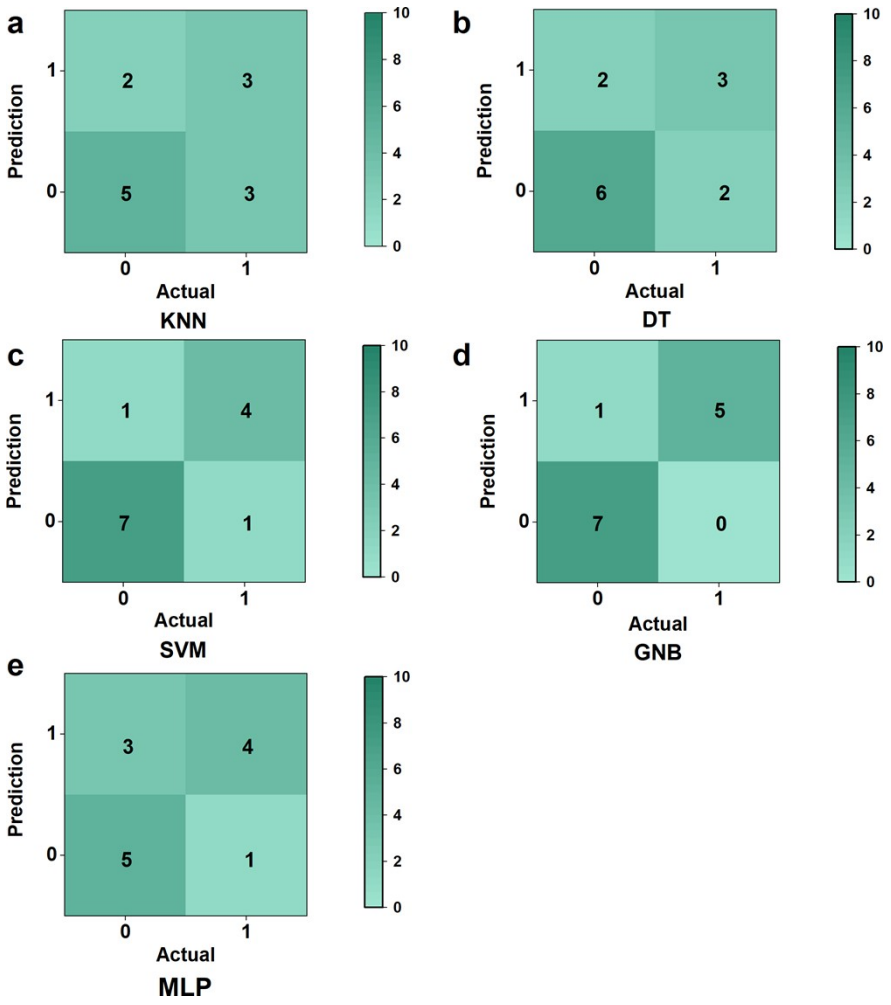

Fig. S1 The confusion matrices of the five ML models for binary classification: (a) k-nearest neighbors (KNN); (b) decision tree (DT); (c) support vector machine (SVM); (d) Gaussian naive Bayes (GNB); (e) multilayer perceptron (MLP)

Based on the confusion matrices in Fig. S1 above, TPR (True Positive Rate) and FPR (False Positive Rate) are calculated and used to assess the predictive accuracy of machine learning in a more detailed manner. Specifically, TPR calculates the proportion of cases where Actual = 1 and Prediction = 1 among all cases where Actual = 1. While FPR calculates the proportion of cases where Actual = 0 but Prediction = 1 among all cases where Actual = 0.

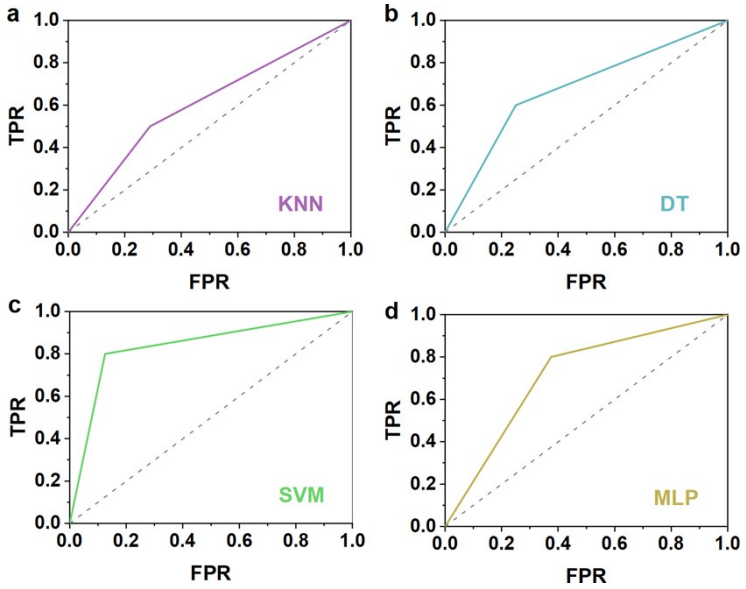

Fig. S2 The ROC curves of the other four ML models. a) k-nearest neighbors (KNN), b) decision tree (DT), c) support vector machine (SVM), d) multilayer perceptron (MLP).

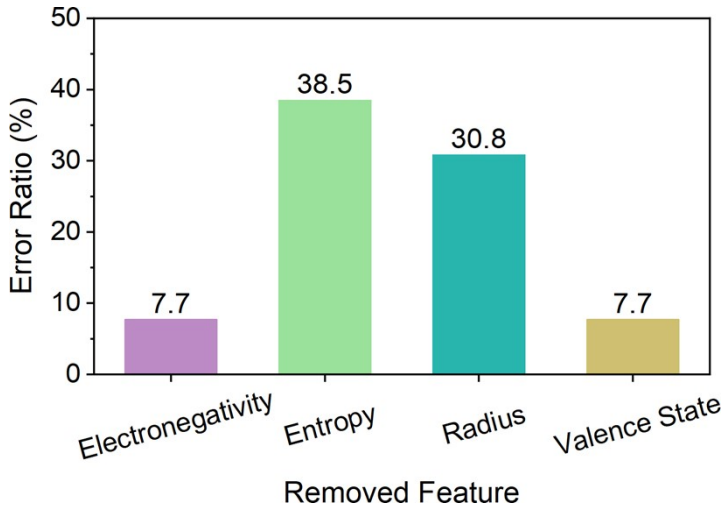

Fig. S3 Results of feature importance analysis: increase in error ratio after removing individual features.

As shown in Fig. S3, the feature importance was evaluated by measuring the increase in model error when each individual descriptor was removed from the training process. A larger increase in error indicates a stronger contribution of that feature to the predictive performance of the model. According to the results, configurational entropy ranks as the most important descriptor. Its removal leads to the largest increase in prediction error, indicating that configurational entropy plays a dominant role in the model. This likely reflects its key influence on structural disorder, phase stability, or property variation in the studied material system. Ionic radius is the second most influential feature. Removing it results in a significant rise in error, though less than that of configurational entropy. This suggests that ionic size substantially affects structural arrangement, lattice strain, or ion-diffusion behavior captured by the model. Valence state and electronegativity show comparable and relatively lower importance, ranking third. Their removal causes a moderate but noticeable increase in error, indicating that both features contribute meaningfully to predictions. Specifically, valence state relates to charge balance and bonding capacity, while electronegativity influences bond polarity and chemical interactions. Nevertheless, their individual effects are less decisive than those of configurational entropy and ionic radius within this specific modeling context.

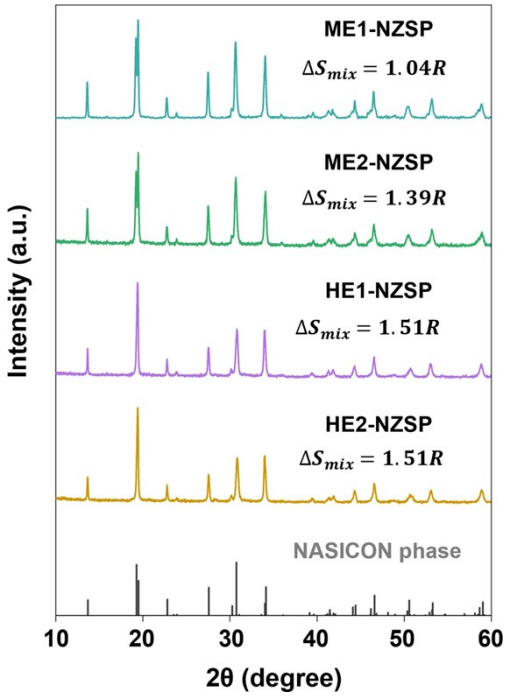

Fig. S4 XRD patterns of four ML-selected medium- to high-entropy NASICON-type oxide SSEs (ME1-NZSP, ME2-NZSP, HE1-NZSP, and HE2-NZSP).

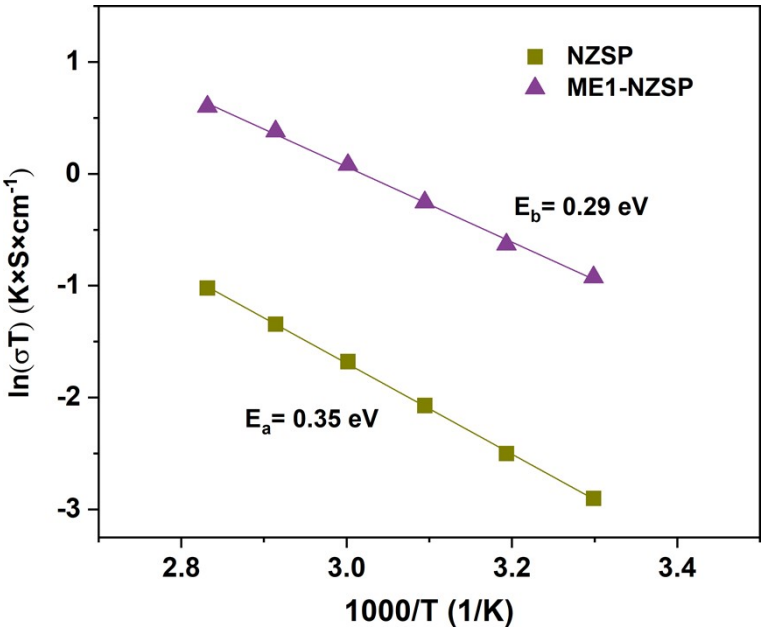

Fig. S5 Arrhenius plots of NZSP and ME1-NZSP SSEs.

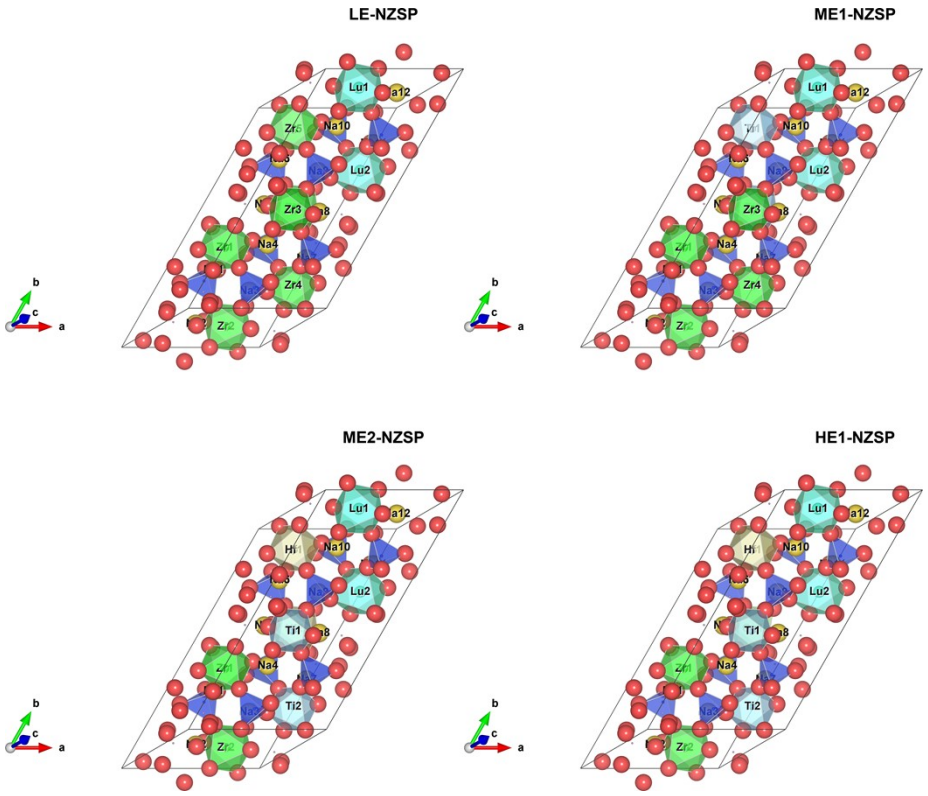

Fig. S6 Structural optimization models of four representative compositions (LE-NZSP, ME1-NZSP, ME2-NZSP, and HE1-NZSP) obtained from DFT calculations.

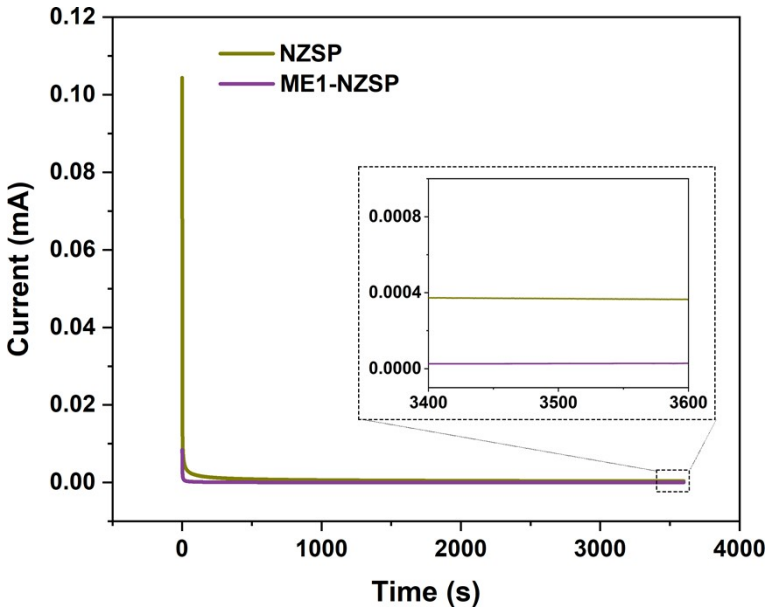

Fig. S7 DC polarization curves of NZSP and ME1-NZSP SSEs.

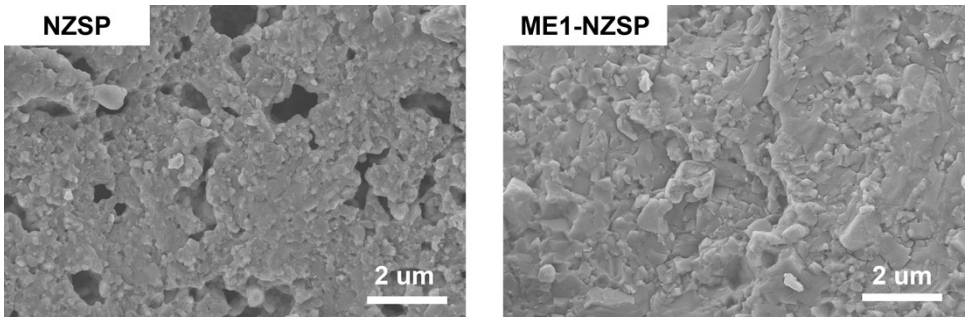

Fig. S8 Cross-sectional SEM images of NZSP and ME1-NZSP SSEs. The NZSP electrolyte exhibits numerous voids in its cross-section, which would facilitate rapid sodium dendrite propagation during cycling. In contrast, ME1-NZSP demonstrates a homogeneous, densely-packed microstructure enabled by entropy-driven stabilization, effectively suppressing sodium dendrite formation.

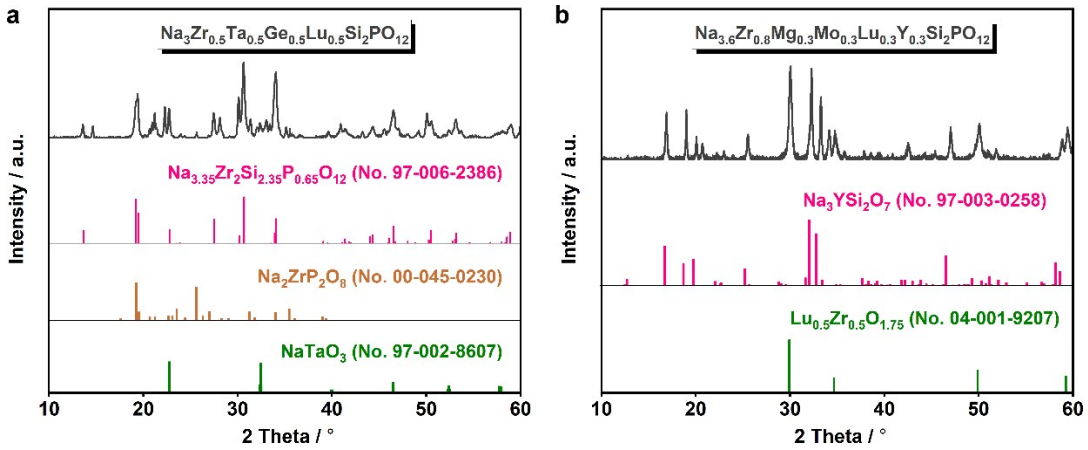

Fig. S9. XRD patterns for two of the compositions that were predicted to be non-synthesizable: (a) $Na_3Zr_{0.5}Ta_{0.5}Ge_{0.5}Lu_{0.5}Si_2PO_{12}$ and (b) $Na_{3.6}Zr_{0.8}Mg_{0.3}Mo_{0.3}Lu_{0.3}Y_{0.3}Si_2PO_{12}$.

Fig. S9a shows the XRD pattern for $Na_3Zr_{0.5}Ta_{0.5}Ge_{0.5}Lu_{0.5}Si_2PO_{12}$, which was predicted to be non-synthesizable. The pattern reveals that the sample is composed primarily of three phases: $Na_{3.35}Zr_2Si_{2.35}P_{0.65}O_{12}$ (No. 97-006-2386), $Na_2ZrP_2O_8$ (No. 00-045-0230), and $NaTaO_3$ (No. 97-002-8607). **Fig. S9b** shows the XRD pattern for $Na_{3.6}Zr_{0.8}Mg_{0.3}Mo_{0.3}Lu_{0.3}Y_{0.3}Si_2PO_{12}$, which was also predicted to be non-synthesizable. The pattern indicates the formation of two main phases: $Na_3YSi_2O_7$ (No. 97-003-0258) and $Lu_{0.5}Zr_{0.5}O_{1.75}$ (No. 04-001-9207). These XRD patterns illustrate the multi-phase nature of the samples that failed to form the intended single-phase NASICON structure, thereby providing insight into the structural outcomes of the unsynthesized compositions.

Supplementary Tables

Table S1. Phase formation results of different component NASICON oxides.

Number	Composition	Entropy value (ΔS_{mix})	Result
1	$Na_{3.2}Zr_{1.9}Ca_{0.1}Si_2PO_{12}$ [3]	0.20R	synthesizable
2	$Na_{3.1}Zr_{1.9}Nd_{0.1}Si_2PO_{12}$ [4]	0.20R	synthesizable
3	$Na_{3.1}Zr_{1.9}Gd_{0.1}Si_2PO_{12}$ [5]	0.20R	synthesizable
4	$Na_{3.1}Zr_{1.9}Yb_{0.1}Si_2PO_{12}$ [5]	0.20R	synthesizable
5	$Na_3Zr_{1.9}Ti_{0.1}Si_2PO_{12}$ [6]	0.20R	synthesizable
6	$Na_{3.4}Mg_{0.2}Zr_{1.8}Si_2PO_{12}$ [7]	0.33R	synthesizable
7	$Na_{3.4}Zr_{1.8}Zn_{0.2}Si_2PO_{12}$ [8]	0.33R	synthesizable
8	$Na_{3.2}Zr_{1.8}Al_{0.2}Si_2PO_{12}$ [9]	0.33R	synthesizable
9	$Na_{3.2}Zr_{1.8}Y_{0.2}Si_2PO_{12}$ [10]	0.33R	synthesizable
10	$Na_{3.3}Zr_{1.7}La_{0.3}Si_2PO_{12}$ [11]	0.42R	synthesizable
11	$Na_{3.4}Zr_{1.6}Sc_{0.4}Si_2PO_{12}$ [12]	0.50R	synthesizable
12	$Na_{3.33}Zr_{1.67}Sc_{0.29}Yb_{0.04}Si_2PO_{12}$ [13]	0.51R	synthesizable
13	$Na_{3.5}Zr_{1.5}Lu_{0.5}Si_2PO_{12}$	0.56R	synthesizable
14	$Na_3ZrSnSi_2PO_{12}$ [14]	0.69R	synthesizable
15	$Na_{3.3}Zr_{1.6}Ta_{0.1}Zn_{0.1}Tm_{0.1}Lu_{0.1}Si_2PO_{12}$	0.78R	non-synthesizable
16	$Na_{3.2}Zr_{1.6}Ta_{0.1}Y_{0.1}Tm_{0.1}Lu_{0.1}Si_2PO_{12}$	0.78R	non-synthesizable
17	$Na_{3.1}Zr_{1.6}Ta_{0.1}Ge_{0.1}Tm_{0.1}Lu_{0.1}Si_2PO_{12}$	0.78R	non-synthesizable
18	$Na_{3.1}Zr_{1.6}Ta_{0.1}Hf_{0.1}Tm_{0.1}Lu_{0.1}Si_2PO_{12}$	0.78R	non-synthesizable
19	$Na_{3.3}Zr_{1.5}Y_{0.1}Hf_{0.1}Ge_{0.1}Tm_{0.1}Lu_{0.1}Si_2PO_{12}$	0.97R	synthesizable
20	$Na_{3.4}Zr_{1.5}Zn_{0.1}Hf_{0.1}Ge_{0.1}Tm_{0.1}Lu_{0.1}Si_2PO_{12}$	0.97R	synthesizable
21	$Na_{3.5}Zr_{1.5}Zn_{0.1}Y_{0.1}Ge_{0.1}Tm_{0.1}Lu_{0.1}Si_2PO_{12}$	0.97R	synthesizable
22	$Na_{3.5}Zr_{1.5}Mg_{0.1}Sn_{0.1}Y_{0.1}Tm_{0.1}Lu_{0.1}Si_2PO_{12}$	0.97R	synthesizable
23	$Na_{3.4}Zr_{1.5}Sc_{0.1}Hf_{0.1}Al_{0.1}Mg_{0.1}Ce_{0.1}Si_2PO_{12}$	0.97R	non-synthesizable
24	$Na_{3.3}Zr_{1.5}Sc_{0.1}Ta_{0.1}Al_{0.1}Mg_{0.1}Ce_{0.1}Si_2PO_{12}$	0.97R	non-synthesizable
25	$Na_{3.4}Zr_{1.5}Zn_{0.1}Ta_{0.1}Y_{0.1}Tm_{0.1}Lu_{0.1}Si_2PO_{12}$	0.97R	non-synthesizable
26	$Na_{3.3}Zr_{1.5}Zn_{0.1}W_{0.1}Y_{0.1}Tm_{0.1}Lu_{0.1}Si_2PO_{12}$	0.97R	non-synthesizable
27	$Na_{3.5}Zr_{1.5}Mg_{0.1}Sn_{0.1}Nd_{0.1}Tm_{0.1}Lu_{0.1}Si_2PO_{12}$	0.97R	non-synthesizable
28	$Na_{3.5}Zr_{1.5}Mg_{0.1}Sn_{0.1}Ga_{0.1}Tm_{0.1}Lu_{0.1}Si_2PO_{12}$	0.97R	synthesizable
29	$Na_{3.5}Zr_{1.5}Sc_{0.1}Ga_{0.1}Y_{0.1}Tm_{0.1}Lu_{0.1}Si_2PO_{12}$	0.97R	synthesizable

Number	Composition	Entropy value (ΔS_{mix})	Result
30	$Na_{3.5}Zr_{1.5}Ca_{0.1}Sn_{0.1}Y_{0.1}Tm_{0.1}Lu_{0.1}Si_2PO_{12}$	0.97R	synthesizable
31	$Na_{3.5}Zr_{1.5}Mg_{0.1}Sn_{0.1}Zn_{0.1}Hf_{0.1}Lu_{0.1}Si_2PO_{12}$	0.97R	synthesizable
32	$Na_{3.5}Zr_{1.4}Zn_{0.1}Y_{0.1}Hf_{0.1}Ge_{0.1}Tm_{0.1}Lu_{0.1}Si_2PO_{12}$	1.15R	synthesizable
33	$Na_{3.5}Sc_{0.5}Ti_{0.5}Zr_{0.5}Hf_{0.5}Si_2PO_{12}$ [15]	1.39R	synthesizable
34	$Na_3Zr_{0.5}Ti_{0.5}Hf_{0.5}Ce_{0.5}Si_2PO_{12}$	1.39R	non-synthesizable
35	$Na_3Zr_{0.5}Ti_{0.5}Hf_{0.5}Ge_{0.5}Si_2PO_{12}$	1.39R	non-synthesizable
36	$Na_4Zr_{0.5}Ti_{0.5}Hf_{0.5}Mg_{0.5}Si_2PO_{12}$	1.39R	non-synthesizable
37	$Na_{3.4}Sc_{0.2}In_{0.2}Ti_{0.2}Zr_{0.7}Hf_{0.7}Si_2PO_{12}$ [15]	1.43R	synthesizable
38	$Na_{3.5}Mg_{0.1}Sc_{0.15}In_{0.15}Ti_{0.3}Hf_{0.3}ZrSi_2PO_{12}$ [15]	1.45R	synthesizable
39	$Na_{3.3}Zr_{0.8}Ti_{0.3}Sn_{0.3}Ir_{0.3}Bi_{0.3}Si_2PO_{12}$	1.51R	non-synthesizable
40	$Na_3Zr_{0.8}Ti_{0.3}Sn_{0.3}Hf_{0.3}Ce_{0.3}Si_2PO_{12}$	1.51R	non-synthesizable
41	$Na_{3.3}Zr_{0.8}Ti_{0.3}Sn_{0.3}Hf_{0.3}Lu_{0.3}Si_2PO_{12}$	1.51R	non-synthesizable
42	$Na_{3.6}Zr_{0.8}Ti_{0.3}Sn_{0.3}Hf_{0.3}Zn_{0.3}Si_2PO_{12}$	1.51R	non-synthesizable
43	$Na_{3.3}Zr_{0.5}Ti_{0.5}Hf_{0.4}Lu_{0.5}W_{0.1}Si_2PO_{12}$	1.51R	non-synthesizable
44	$Na_{3.3}Zr_{0.5}Ti_{0.5}Hf_{0.4}Lu_{0.5}Mo_{0.1}Si_2PO_{12}$	1.51R	non-synthesizable
45	$Na_{3.4}Zr_{0.4}Ti_{0.4}Sn_{0.4}Ir_{0.4}Bi_{0.4}Si_2PO_{12}$	1.61R	non-synthesizable
46	$Na_3Zr_{0.4}Ti_{0.4}Sn_{0.4}Hf_{0.4}Ce_{0.4}Si_2PO_{12}$	1.61R	non-synthesizable
47	$Na_{3.4}Zr_{0.4}Ti_{0.4}Sn_{0.4}Hf_{0.4}Lu_{0.4}Si_2PO_{12}$	1.61R	non-synthesizable
48	$Na_{3.8}Zr_{0.4}Ti_{0.4}Sn_{0.4}Hf_{0.4}Zn_{0.4}Si_2PO_{12}$	1.61R	non-synthesizable
49	$Na_{3.4}Zr_{0.4}Zn_{0.4}Sn_{0.4}Hf_{0.4}Ta_{0.4}Si_2PO_{12}$	1.61R	non-synthesizable
50	$Na_{4.6}Zr_{0.4}Zn_{0.4}Sn_{0.4}Hf_{0.4}Mg_{0.4}Si_2PO_{12}$	1.61R	non-synthesizable
51	$Na_{4.6}Zr_{0.4}Tm_{0.4}Sn_{0.4}Mg_{0.4}Lu_{0.4}Si_2PO_{12}$	1.61R	non-synthesizable
52	$Na_{4.2}Zr_{0.4}Tm_{0.4}Sn_{0.4}Y_{0.4}Lu_{0.4}Si_2PO_{12}$	1.61R	non-synthesizable
53	$Na_{4.6}Zr_{0.4}Y_{0.4}Tm_{0.4}Yb_{0.4}Lu_{0.4}Si_2PO_{12}$	1.61R	non-synthesizable
54	$Na_{4.2}Zr_{0.4}Zn_{0.4}Sn_{0.4}Hf_{0.4}Lu_{0.4}Si_2PO_{12}$	1.61R	non-synthesizable
55	$Na_{3.0}Zr_{0.4}Bi_{0.4}Sn_{0.4}Hf_{0.4}Ta_{0.4}Si_2PO_{12}$	1.61R	non-synthesizable
56	$Na_{4.6}Zr_{0.4}Tm_{0.4}Sn_{0.4}Zn_{0.4}Lu_{0.4}Si_2PO_{12}$	1.61R	non-synthesizable
57	$Na_{3.4}Zr_{0.4}Tm_{0.4}Sn_{0.4}Nb_{0.4}Lu_{0.4}Si_2PO_{12}$	1.61R	non-synthesizable
58	$Na_{4.6}Zr_{0.4}Er_{0.4}Tm_{0.4}Yb_{0.4}Lu_{0.4}Si_2PO_{12}$	1.61R	non-synthesizable

Table S2. The four eigenvalues of machine learning.

Number	Ionic radius (ppm)	Electronegativity	Valence state (+)	Entropy (×R)
1	84.80	1.314	3.90	0.199
2	84.72	1.321	3.95	0.199
3	84.49	1.324	3.95	0.199
4	84.14	1.325	3.95	0.199
5	82.83	1.341	4.00	0.199
6	82.80	1.328	3.80	0.325
7	81.60	1.362	3.80	0.325
8	80.95	1.358	3.90	0.325
9	84.60	1.319	3.90	0.325
10	86.88	1.296	3.85	0.423
11	82.10	1.336	3.80	0.500
12	82.68	1.332	3.84	0.509
13	84.53	1.248	3.75	0.562
14	76.50	1.645	4.00	0.693
15	82.11	1.334	3.85	0.778
16	83.61	1.313	3.90	0.778
17	81.76	1.352	3.95	0.778
18	83.26	1.317	3.95	0.778
19	83.01	1.337	3.85	0.965
20	81.51	1.358	3.80	0.965
21	81.86	1.354	3.75	0.965
22	83.26	1.335	3.75	0.965
23	82.00	1.333	3.80	0.965
24	81.05	1.343	3.85	0.960
25	82.41	1.329	3.80	0.965
26	82.21	1.339	3.85	0.965
27	83.67	1.331	3.75	0.965
28	81.86	1.364	3.75	0.965
29	83.03	1.330	3.75	0.965
30	84.66	1.319	3.75	0.965
31	81.51	1.359	3.75	0.965
32	81.81	1.353	3.75	1.148
33	75.50	1.383	3.75	1.386
34	81.13	1.323	4.00	1.386

Number	Ionic radius (ppm)	Electronegativity	Valence state (+)	Entropy (×R)
35	70.13	1.545	4.00	1.386
36	74.88	1.370	3.50	1.386
37	79.95	1.389	3.80	1.426
38	78.71	1.392	3.75	1.454
39	77.85	1.672	3.85	1.505
40	80.03	1.420	4.00	1.505
41	78.39	1.402	3.85	1.505
42	74.48	1.500	3.70	1.505
43	77.25	1.313	3.85	1.511
44	77.20	1.336	3.85	1.511
45	75.80	1.786	3.80	1.609
46	78.70	1.450	4.00	1.609
47	76.52	1.426	3.80	1.609
48	71.30	1.556	3.60	1.609
49	72.00	1.548	3.80	1.609
50	73.60	1.510	3.20	1.609
51	79.82	1.370	3.20	1.609
52	83.42	1.352	3.40	1.609
53	86.98	1.204	3.20	1.609
54	76.42	1.448	3.40	1.609
55	80.60	1.598	4.00	1.609
56	77.42	1.438	3.20	1.609
57	78.22	1.428	3.80	1.609
58	86.78	1.208	3.20	1.609

Table S3. List of the twelve medium- and high-entropy NASICON oxides predicted using a machine learning approach.

Number	Composition	Entropy value (ΔS_{mix})	Predicted Results	Experimental Results
1	$Na_{3.5}Zr_{1.0}Ti_{0.5}Lu_{0.5}Si_2PO_{12}$	1.04R	synthesizable	synthesizable
2	$Na_3Zr_{1.0}Mo_{0.5}Mg_{0.5}Si_2PO_{12}$	1.04R	non-synthesizable	non-synthesizable
3	$Na_{3.5}Zr_{1.0}Sn_{0.5}Lu_{0.5}Si_2PO_{12}$	1.04R	synthesizable	non-synthesizable
4	$Na_{3.5}Zr_{1.0}Nb_{0.5}Zn_{0.5}Si_2PO_{12}$	1.04R	non-synthesizable	non-synthesizable
5	$Na_3Zr_{1.0}Sc_{0.5}Ta_{0.5}Si_2PO_{12}$	1.04R	non-synthesizable	non-synthesizable
6	$Na_{3.5}Zr_{0.5}Ti_{0.5}Hf_{0.5}Lu_{0.5}Si_2PO_{12}$	1.39R	synthesizable	synthesizable
7	$Na_3Zr_{0.5}Ta_{0.5}Ge_{0.5}Lu_{0.5}Si_2PO_{12}$	1.39R	non-synthesizable	non-synthesizable
8	$Na_{3.5}Zr_{0.5}Ta_{0.5}Al_{0.5}Lu_{0.5}Si_2PO_{12}$	1.39R	non-synthesizable	non-synthesizable
9	$Na_{3.6}Zr_{0.8}Mg_{0.3}Mo_{0.3}Lu_{0.3}Y_{0.3}Si_2PO_{12}$	1.51R	non-synthesizable	non-synthesizable
10	$Na_{3.6}Zr_{0.8}Yb_{0.3}Nb_{0.3}Lu_{0.3}Y_{0.3}Si_2PO_{12}$	1.51R	non-synthesizable	non-synthesizable
11	$Na_{3.6}Zr_{0.5}Ti_{0.5}Hf_{0.4}Lu_{0.5}Ga_{0.1}Si_2PO_{12}$	1.51R	synthesizable	synthesizable
12	$Na_{3.6}Zr_{0.5}Ti_{0.5}Hf_{0.4}Lu_{0.5}Sc_{0.1}Si_2PO_{12}$	1.51R	synthesizable	synthesizable

Table S4. Rietveld refinement structural parameters for the medium-entropy composition $Na_{3.5}Zr_{1.0}Ti_{0.5}Lu_{0.5}Si_2PO_{12}$.

$Na_{3.49}Zr_{1.0}Ti_{0.5}Lu_{0.5}Si_2PO_{12}$ (*C*2/*c*)						
Atomic Occupancies	Wyckoff	Atom	x	y	z	Occ.
	4e	Na	0.50000	0.91401	0.25000	0.54371
	4d	Na	0.25000	0.25000	0.50000	0.43493
	8f	Na	0.84540	-0.10553	0.61367	0.60878
	4e	P	0.00000	0.11548	0.25000	0.17000
	4e	Si	0.00000	0.11548	0.25000	0.33000
	8f	P	0.34082	0.12246	0.21362	0.33000
	8f	Si	0.34082	0.12246	0.21362	0.67000
	8f	Zr	0.09514	0.24140	0.05174	0.50000
	8f	Ti	0.09514	0.24140	0.05174	0.25000
	8f	Lu	0.09514	0.24140	0.05174	0.25000
	8f	O	0.08906	0.11101	0.28901	1.00000
	8f	O	0.49128	0.21453	0.43050	1.00000
	8f	O	0.10907	0.45827	0.22016	1.00000
	8f	O	0.30030	0.19213	-0.00104	1.00000
	8f	O	0.43418	0.47603	0.09113	1.00000
	8f	O	0.27691	0.19555	0.25112	1.00000
Lattice Parameters	a/Å		b/Å		c/Å	
	15.61382		9.04419		9.19836	

Table S5. Rietveld refinement structural parameters for the medium-entropy composition $Na_{3.5}Zr_{0.5}Ti_{0.5}Hf_{0.5}Lu_{0.5}Si_2PO_{12}$.

$Na_{3.48}Zr_{0.5}Ti_{0.5}Hf_{0.5}Lu_{0.5}Si_2PO_{12}$ (*C*2/*c*)						
Atomic Occupancies	Wyckoff	Atom	x	y	z	Occ.
	4e	Na	0.50000	0.94107	0.25000	0.45639
	4d	Na	0.25000	0.25000	0.50000	0.41307
	8f	Na	0.77681	0.07491	0.69792	0.63054
	4e	P	0.00000	0.02263	0.25000	0.17000
	4e	Si	0.00000	0.02263	0.25000	0.33000
	8f	P	0.33956	0.12052	0.26148	0.33000
	8f	Si	0.33956	0.12052	0.26148	0.67000
	8f	Zr	0.09820	0.24446	0.05561	0.25000
	8f	Ti	0.09820	0.24446	0.05561	0.25000
	8f	Hf	0.09820	0.24446	0.05561	0.25000
	8f	Lu	0.09820	0.24446	0.05561	0.25000
	8f	O	0.08725	0.11518	0.24193	1.00000
	8f	O	0.45991	0.17055	0.41622	1.00000
	8f	O	0.18611	0.48210	0.25985	1.00000
	8f	O	0.42150	0.05521	0.13639	1.00000
	8f	O	0.41223	0.46852	0.02318	1.00000
	8f	O	0.23481	0.14548	0.17267	1.00000
Lattice Parameters	a/Å		b/Å		c/Å	
	15.60013		9.03673		9.19456	

Table S6. Rietveld refinement structural parameters for the high-entropy composition $Na_{3.6}Zr_{0.5}Ti_{0.5}Hf_{0.4}Lu_{0.5}Ga_{0.1}Si_2PO_{12}$.

$Na_{3.59}Zr_{0.5}Ti_{0.5}Hf_{0.4}Lu_{0.5}Ga_{0.1}Si_2PO_{12}$ (*C*2/*c*)						
Atomic Occupancies	Wyckoff	Atom	x	y	z	Occ.
	4e	Na	0.50000	0.83682	0.25000	0.86129
	4d	Na	0.25000	0.25000	0.50000	0.22167
	8f	Na	0.86932	0.28761	0.83424	0.41704
	4e	P	0.00000	0.09051	0.25000	0.17000
	4e	Si	0.00000	0.09051	0.25000	0.33000
	8f	P	0.34306	0.09958	0.20092	0.33000
	8f	Si	0.34306	0.09958	0.20092	0.67000
	8f	Zr	0.10557	0.25211	0.05306	0.12500
	8f	Ti	0.10557	0.25211	0.05306	0.12500
	8f	Hf	0.10557	0.25211	0.05306	0.10000
	8f	Lu	0.10557	0.25211	0.05306	0.12500
	8f	Ga	0.10557	0.25211	0.05306	0.02500
	8f	O	0.08564	0.07055	0.25521	1.00000
	8f	O	0.47742	0.18375	0.42427	1.00000
	8f	O	0.20403	0.47440	0.20928	1.00000
	8f	O	0.26216	0.18469	-0.04374	1.00000
	8f	O	0.44311	0.61171	0.20092	1.00000
	8f	O	0.31675	0.18507	0.28294	1.00000
Lattice Parameters	a/Å		b/Å		c/Å	
	15.60500		9.01500		9.18000	

Table S7. Rietveld refinement structural parameters for the high-entropy composition $Na_{3.6}Zr_{0.5}Ti_{0.5}Hf_{0.4}Lu_{0.5}Sc_{0.1}Si_2PO_{12}$.

$Na_{3.62}Zr_{0.5}Ti_{0.5}Hf_{0.4}Lu_{0.5}Sc_{0.1}Si_2PO_{12}$ (*C*2/*c*)						
Atomic Occupancies	Wyckoff	Atom	x	y	z	Occ.
	4e	Na	0.50000	0.89396	0.25000	0.50388
	4d	Na	0.25000	0.25000	0.50000	0.26094
	8f	Na	0.79758	0.22482	0.80429	0.73518
	4e	P	0.00000	0.02414	0.25000	0.17000
	4e	Si	0.00000	0.02414	0.25000	0.33000
	8f	P	0.36316	0.12585	0.25134	0.33000
	8f	Si	0.36316	0.12585	0.25134	0.67000
	8f	Zr	0.09598	0.25353	0.06155	0.12500
	8f	Ti	0.09598	0.25353	0.06155	0.12500
	8f	Hf	0.09598	0.25353	0.06155	0.10000
	8f	Lu	0.09598	0.25353	0.06155	0.12500
	8f	Sc	0.09598	0.25353	0.06155	0.02500
	8f	O	0.08458	0.13769	0.30390	1.00000
	8f	O	0.46507	0.21530	0.42909	1.00000
	8f	O	0.12205	0.42329	0.18746	1.00000
	8f	O	0.24810	0.10965	-0.10503	1.00000
	8f	O	0.42869	0.45543	0.03138	1.00000
	8f	O	0.23718	0.15027	0.16179	1.00000
Lattice Parameters	a/Å		b/Å		c/Å	
	15.62000		9.03000		9.19000	

Table S8. The bulk (σ_b), grain-boundary (σ_{gb}) and total (σ_t) ionic conductivities of $Na_{3.5}Zr_{1.0}Ti_{0.5}Lu_{0.5}Si_2PO_{12}$ (ME1-NZSP) and $Na_3Zr_2Si_2PO_{12}$ (NZSP) pellets.

	ME1-NZSP	NZSP
σ_b (mS cm^{-1})	2.95	2.98
σ_{gb} (mS cm^{-1})	2.16	0.29
σ_t (mS cm^{-1})	1.30	0.26

As shown in **Table S8**, both materials exhibit comparable bulk ionic conductivities (~2.95-2.98 mS cm^{-1}). The most notable improvement is observed in the grain-boundary conductivity. σ_{gb} for ME1-NZSP (2.16 mS cm^{-1}) is ~7.4 times higher than that of the undoped NZSP (0.29 mS cm^{-1}). This dramatic increase is the primary reason for the superior total ionic conductivity of ME1-NZSP. Therefore, although the bulk conductivities are similar, the vastly improved grain-boundary conductivity directly results in ME1-NZSP achieving a total ionic conductivity (1.30 mS cm^{-1}) that is approximately 5 times higher than that of baseline NZSP (0.26 mS cm^{-1}).

Table S9. Shrinkage rates and relative densities of the pristine NZSP and ME1-NZSP pellets

Sample	$D_{(pre\text{-}sintered)}$ (mm)	$D_{(sintered)}$ (mm)	Shrinkage rates (%)	$\rho_{(measured)}$ (g/cm^3)	$\rho_{(theoretical)}$ (g/cm^3)	Relative Density(%)
NZSP	10	9.91	0.9	2.776	3.243	85.6
ME1-NZSP	10	8.56	14.4	3.361	3.437	97.8

*Note: The linear shrinkage rate was calculated as $[(D_{(pre\text{-}sintered)} - D_{(sintered)}) / D_{(pre\text{-}sintered)}] \times 100\%$. The relative density was determined using the Archimedes (water immersion) method, expressed as $(\rho_{(measured)} / \rho_{(theoretical)}) \times 100\%$.

The key parameters are summarized in **Table S9** above. The pristine NZSP pellet exhibited a low linear shrinkage of 0.9% and a correspondingly low relative density of 85.6%, indicating insufficient densification during sintering. In contrast, the ME1-NZSP pellet showed a significantly higher linear shrinkage of 14.4%, which contributed to its achieving a near-fully dense structure with a relative density of 97.8%.

Table S10. Comparative electrochemical performance of solid-state sodium metal batteries employing NZSP-type NASICON oxide SSEs from literature reports.

Oxide SSEs	Cathode	Rate, temperature	Cycle number	Initial capacity (mAh/g)	Last capacity (mAh/g)	Ref.
$Na_{3.125}Zr_{1.75}Sc_{0.125}Ge_{0.125}Si_2PO_{12}$	NVP	0.2C, R.T.	250	101.0	98.9	[16]
$Na_3Zr_2Si_2PO_{12}$	NVP	0.5C, 80℃	100	92.3	75.7	[17]
$Na_3Zr_2Si_2PO_{12}$	NVP	0.1C, 80℃	120	103.9	97.6	[18]
Mg/F-$Na_3Zr_2Si_2PO_{12}$	NVP	0.2C, R.T.	50	95.0	85.7	[19]
$Na_3Zr_2Si_2PO_{12}$-0.7F	NVP	0.5C, 40℃	100	87.8	85.9	[20]
$Na_3Zr_2Si_2PO_{12}$	NVP	10μA/cm^2, 80℃	50	80.0	53.0	[21]
$Na_{3.4}Mg_{0.1}Zr_{1.9}Si_{2.2}P_{0.8}O_{12}$	NVP	0.1C, 60℃	50	100.0	93.3	[22]
$Na_3Zr_2Si_2PO_{12}$-3BTO	NVCP	100 mA g^{-1}, 25℃	400	95.0	81.0	[23]
0.2Mg-$Na_3Zr_2Si_2PO_{12}$	$NaCrO_2$	5.0C, 25℃	470	102.6	88.4	[24]
$Na_3Zr_2Si_2PO_{12}$	NVP	0.5C, R.T.	100	96.7	91.1	[25]
$Na_3Zr_2Si_2PO_{12}$	NVP	1.0C, 30℃	400	64.6	19.4	[26]
$Na_{3.65}Zr_{1.675}Zn_{0.2}Mg_{0.125}Si_2PO_{12}$	NVP	0.2C, R.T.	300	116	76.6	[27]
$Na_{3.36}Zr_{1.64}Sc_{0.36}Si_2PO_{12}$	NVP	1.0C, 30℃	350	108.8	97.3	[28]
α-FeOF@$Na_3Zr_2Si_2PO_{12}$	NVP	2.0C, 80℃	500	89.6	66.3	[29]
$Na_3Zr_2Si_2PO_{12}$-SPAN	NVP	0.5C, R.T.	200	104.8	87.5	[30]
$Na_3Zr_2Si_2PO_{12}$	NVCP	100 mA g^{-1}, 25℃	400	103	75.2	[31]
TiO_2-$Na_3Zr_2Si_2PO_{12}$	NVP	0.1C, 60℃	60	106.3	75.0	[32]
$Na_{3.4}Zr_{1.8}Mn_{0.2}Si_2PO_{12}$	NVP	0.1C, 25℃	260	91.3	84.2	[33]
$Na_{3.2}Zr_{1.8}Ce_{0.2}Si_2PO_{12}$	NVP	0.5C, 25℃	200	111.2	109.0	[34]
SnF_2-$Na_3Zr_2Si_2PO_{12}$	NVP	1.0C, 25℃	200	110.3	72.2	[35]
ME1-NZSP	NVPF	2.0C, R.T.	700	113.3	90.6	This work

Note: NVP = $Na_3V_2(PO_4)_3$, R.T. = Room temperature, NVCP = $Na_3V_{1.5}Cr_{0.5}(PO_4)_3$, NVPF = $Na_3V_2(PO_4)_2F_3$, ME1-NZSP = $Na_{3.5}Zr_{0.5}Ti_{0.5}Hf_{0.5}Lu_{0.5}Si_2PO_{12}$

References

1. H. Gao, L. Xue, S. Xin, K. Park, J.B. Goodenough, *Angew.Chem. Int. Ed.*, 2017, **56**, 5541-5545.
2. D. Li, C. Sun, C. Wang, J. Li, Z. Wang, H. Jin, *Energy Storage Mater.*, 2023, **54**, 403-409.
3. Y. Lu, J.A. Alonso, Q. Yi, L. Lu, Z.L. Wang, C. Sun, *Adv. Energy Mater.*, 2019, **9**, 1901205.
4. Y. Ruan, S. Song, J. Liu, P. Liu, B. Cheng, X. Song, V. Battaglia, *Ceram. Int.*, 2017, **43**, 7810-7815.
5. Z. Khakpour, *Electrochim. Acta*, 2016, **196**, 337-347.
6. D. Chen, F. Luo, W. Zhou, D. Zhu, *J. Alloys Compd.*, 2018, **757**, 348-355.
7. C. Wang, Z. Sun, Y. Zhao, B. Wang, C. Shao, C. Sun, Y. Zhao, J. Li, H. Jin, L. Qu, small, 2021, **17**, 2103819.
8. J. Yang, G. Liu, M. Avdeev, H. Wan, F. Han, L. Shen, Z. Zou, S. Shi, Y. Hu, C. Wang, X. Yao, *ACS Energy Lett.*, 2020, **5**, 2835-2841.
9. A.G. Jolley, G. Cohn, G.T. Hitz, E.D. Wachsman, *Ionics*, 2015, **21**, 3031-3038.
10. Q. Zhang, F. Liang, T. Qu, Y. Yao, W. Ma, B. Yang, Y. Dai, *IOP Conf. Ser. Mater. Sci. Eng.*, 2018, **423**, 012122.
11. Z. Zhang, Q. Zhang, J. Shi, Y.S. Chu, X. Yu, K. Xu, M. Ge, H. Yan, W. Li, L. Gu, Y. Hu, H. Li, X. Yang, L. Chen, X. Huang, *Adv. Energy Mater.*, 2016, **7**, 1601196.
12. Q. Ma, M. Guin, S. Naqash, C. Tsai, F. Tietz, O. Guillon, *Chem. Mater.*, 2016, **28**, 4821-4828.
13. S. K. Pal, R. Saha, G.V. Kumar, S. Omar, *J. Phys. Chem. C*, 2020, **124**, 9161-9169.
14. P. Yadav, M.C. Bhatnagar, *J. Electroceram.*, 2013, **30**, 145-151.
15. Y. Zeng, B. Ouyang, J. Liu, Y. W. Byeon, Z. Cai, L. Miara, Y. Wang, G. Ceder, *Science*, 2022, **378**, 1320-1324.
16. L. Ran, A. Baktash, M. Li, Y. Yin, B. Demir, T. Lin, M. Li, M. Rana, I. Gentle, L. Wang, D. Searles, R. Knibbe, *Energy Storage Mater.*, 2021, **40**, 282-291.
17. X. Wang, Z. Liu, Y. Tang, J. Chen, D. Wang, Z. Mao, *J. Power Sources*, 2021, **481**, 228924.
18. Z. Zhang, S. Wenzel, Y. Zhu, J. Sann, L. Shen, J. Yang, X. Yao, Y.-S. Hu, C. Wolverton, H. Li, L. Chen, J. Janek, *ACS Appl. Energy Mater.*, 2020, **3**, 7427-7437.
19. S. He, Y. Xu, X. Ma, Y. Chen, J. Lin, C. Wang, *ChemElectroChem*, 2020, **7**, 2087-2094.
20. S. He, Y. Xu, Y. Chen, X. Ma, *J. Mater. Chem. A*, 2020, **8**, 12594-12602.
21. Y. Noguchi, E. Kobayashi, L.S. Plashnitsa, S. Okada, J.-i. Yamaki, *Electrochim. Acta*, 2013, **101**, 59-65.
22. L. Shen, J. Yang, G. Liu, M. Avdeev, X. Yao, *Mater. Today Energy*, 2021, **20**, 100691.
23. Z. Sun, Y. Zhao, Q. Ni, Y. Liu, C. Sun, J. Li, H. Jin, *Small*, 2022, **18**, 2200716.
24. C. Wang, Z. Sun, Y. Zhao, B. Wang, C. Shao, C. Sun, Y. Zhao, J. Li, H. Jin, L. Qu, *Small*, 2021, **17**, 2103819.
25. X. Wang, J. Chen, Z. Mao, D. Wang, *Chem. Eng. J.*, 2022, **427**, 130899.
26. D. Fang, Y. Li, C. Wang, R. Miao, S. Yang, Y. Zhao, Y. Ding, J. He, L. Chen, N. Li, J. Li, Y. Su, H. Jin, *Energy Storage Mater.*, 2025, **74**, 103973.
27. P. Jaschin, C. Tang, E. Wachsman, *Energy Environ. Sci.*, 2024, **17**, 727-737.
28. H. Liu, Y. Xing, N. Chen, J. Wu, Y. Li, C. Zhang, *Chem. Mater.*, 2023, **35**, 8686-8694.
29. L. Xiang, D. Jiang, Y. Gao, C. Zhang, X. Ren, L. Zhu, S. Gao, X. Zhan, *Adv. Funct. Mater.*, 2024, **34**, 2301670.
30. X. Miao, H. Wang, R. Sun, X. Ge, D. Zhao, P. Wang, R. Wang, L. Yin, *Adv. Energy Mater.*, 2021, **11**, 2003469.

31. C. Wang, H. Jin, Y. Zhao, *Small*, 2021, **17**, 2100974.
32. J. Yang, Z. Gao, T. Ferber, H. Zhang, C. Guhl, L. Yang, Y. Li, Z. Deng, P. Liu, C. Cheng, R. Che, W. Jaegermann, R. Hausbrand, Y. Huang, *J. Mater. Chem. A*, 2020, **8**, 7828-7835.
33. Y. Zhang, T. Gao, J. Yu, Y. Zhang, Y. Zhang, S. Chen, N. Xue, X. Zhang, Q. Yuan, L. Wang, W. Liu, *ACS Appl. Mater. Interfaces*, 2025, **17**, 10722-10731.
34. J. Liu, Z. Xia, Y. Chen, D. Tao, Q. Zhang, *J. Adv. Ceram.*, 2025, **14**, 9221023.
35. T. Li, B. Chen, T. Wang, C. Liu, W. Yin, Q. Mao, D. Zhou, Y. Hao, X. Liu, *Nat. Commun.*, 2025, **16**, 5668.